PNAS RESEARCH ARTICLE | BIOPHYSICS AND COMPUTATIONAL BIOLOGY OPEN ACCESS

Friction-driven membrane scission by the human ESCRT-III proteins CHMP1B and IST1

A. King Cada[a,b], Mark R. Pavlin[b,c], Juan P. Castillo[b,d,1], Alexander B. Tong[b,d], Kevin P. Larsen[a,b], Xuefeng Ren[a,b], Adam L. Yokom[a,b], Feng-Ching Tsai[e], Jamie V. Shiah[a,b], Patricia M. Bassereau[e], Carlos J. Bustamante[a,b,c,d,f,g,h,2], and James H. Hurley[a,b,c,i,2]

Contributed by James H. Hurley; received March 14, 2022; accepted May 31, 2022; reviewed by Phyllis I. Hanson and Jeanne C. Stachowiak

The endosomal sorting complexes required for transport (ESCRT) system is an ancient and ubiquitous membrane scission machinery that catalyzes the budding and scission of membranes. ESCRT-mediated scission events, exemplified by those involved in the budding of HIV-1, are usually directed away from the cytosol ("reverse topology"), but they can also be directed toward the cytosol ("normal topology"). The ESCRT-III subunits CHMP1B and IST1 can coat and constrict positively curved membrane tubes, suggesting that these subunits could catalyze normal topology membrane severing. CHMP1B and IST1 bind and recruit the microtubule-severing AAA$^+$ ATPase spastin, a close relative of VPS4, suggesting that spastin could have a VPS4-like role in normal-topology membrane scission. Here, we reconstituted the process in vitro using membrane nanotubes pulled from giant unilamellar vesicles using an optical trap in order to determine whether CHMP1B and IST1 are capable of membrane severing on their own or in concert with VPS4 or spastin. CHMP1B and IST1 copolymerize on membrane nanotubes, forming stable scaffolds that constrict the tubes, but do not, on their own, lead to scission. However, CHMP1B–IST1 scaffolded tubes were severed when an additional extensional force was applied, consistent with a friction-driven scission mechanism. We found that spastin colocalized with CHMP1B-enriched sites but did not disassemble the CHMP1B–IST1 coat from the membrane. VPS4 resolubilized CHMP1B and IST1 without leading to scission. These observations show that the CHMP1B–IST1 ESCRT-III combination is capable of severing membranes by a friction-driven mechanism that is independent of VPS4 and spastin.

ESCRT | optical tweezers | friction-driven scission | endosome | spastin

Significance

How organelles and vesicles are severed to generate daughter structures is a major question in membrane biology. The ESCRTs CHMP1 and IST1 were previously shown by cryo-EM to tightly constrict tubes, leading to the hypothesis that they could mediate severing of tubular endosomes. We determined that the activity of the VPS4 and spastin ATPases is insufficient to trigger scission. We show that membrane scission does occur under dynamical tube extension, showing that friction-driven scission is operative under these conditions, consistent with a biological role for CHMP1B and IST1 in tubular endosome severing.

The endosomal sorting complexes required for transport (ESCRT) proteins are an ancient and conserved membrane remodeling machinery, present in two of the three domains of life, the Archaea and Eukaryota. In humans, the ESCRTs are involved in myriad cell biological processes (1, 2) ranging from multivesicular body biogenesis (3), cytokinetic abscission (4), membrane repair (5–8), and exosome (9) and HIV-1 release (10, 11). The underlying commonality of most of these processes is that they are topologically equivalent, with scission occurring on the cytosolic and inner surface of a narrow membrane neck ("reverse topology"). The ESCRTs consist of ALIX, ESCRT-0, ESCRT-I, ESCRT-II, ESCRT-III, and VPS4 (12, 13). The ESCRT-III proteins (14) are most directly involved in catalyzing membrane scission (15, 16). These ESCRTs are first recruited to the neck, then the AAA$^+$ ATPase VPS4 (17) is finally recruited to ESCRT-III–enriched sites prior to scission (18). VPS4 forms a hexamer (19, 20) that interacts with ESCRT-III through its N-terminal microtubule-interacting and trafficking (MIT) domain binding to the exposed C-terminal MIT domain interacting motif (MIM) domains found in some ESCRT-III proteins (21, 22). ESCRT-III together with VPS4 constitutes the minimal module to drive scission of vesicles that bud away from the cytosol (16). While ESCRTs are best known for reverse-topology membrane scission, a subset of ESCRTs, CHMP1B and IST1, can also coat the outer surface of membrane tubes, leading to a dramatic constriction in the tube (23, 24). This process is implicated in tubular endosomal traffic from the endoplasmic reticulum (ER) to lysosomes (25–27) and lipid droplets to peroxisomes (28) and the release of newly formed peroxisomes from the ER (29). These observations suggested that CHMP1B and IST1 could carry out normal topology scission; however, direct observation of this type of scission has not been reported.

Twelve different ESCRT-III proteins are found in humans, which can combine in various compositions that nucleate and grow on membranes of various curvatures (23, 30, 31). ESCRT-III proteins are monomeric and are highly basic and share similar secondary core structures containing five helices (32). These proteins are in an autoinhibited closed conformation in solution (33, 34). Activation can be triggered upon

Author contributions: A.K.C., M.R.P., P.M.B., C.J.B., and J.H.H. designed research; A.K.C., M.R.P., A.L.Y., F.-C.T., and J.V.S. performed research; A.K.C., M.R.P., J.P.C., A.B.T., K.P.L., X.R., and J.V.S. contributed new reagents/analytic tools; A.K.C. and J.H.H. analyzed data; A.K.C., P.M.B., and J.H.H. wrote the paper; and J.H.H. supervised research.

Reviewers: P.I.H., University of Michigan; and J.C.S., The University of Texas at Austin.

Competing interest statement: J.H.H. is a co-founder and shareholder of Casma Therapeutics and receives research funding from Casma Therapeutics, Genentech, and Hoffmann-La Roche. J.H.H. and Phyllis Hanson are co-authors on a 2021 paper on guidelines for the autophagy field, and P.M.B. and Jeanne Stachowiak are co-authors on a 2018 multiauthor membrane remodeling roadmap review.

[1]Present address: Soft Matter and Technology Center, Departamento de Física, Facultad de Ciencia, Universidad de Santiago, Santiago, 9170022, Chile.

[2]To whom correspondence may be addressed. Email: carlosb@berkeley.edu or jimhurley@berkeley.edu.

This article contains supporting information online at http://www.pnas.org/lookup/suppl/doi:10.1073/pnas.2204536119/-/DCSupplemental.

Published July 11, 2022.

binding to membranes or upstream activators, or artificially through truncation of their C-terminal elements (33, 34). Upon activation, ESCRT-III proteins polymerize into spirals (35–37) and helical tubes (24, 38). Incubation of CHMP1B with liposomes leads to formation of protein-coated tubules in vitro as shown using cryoelectron microscopy (cryo-EM) (23). This positively curved coat was initially unexpected in the ESCRT field, but subsequently has been observed more generally with combinations of CHMP2, 3, and 4 (39, 40).

In reverse-topology scission, the ATPase activity of VPS4 is essential for the remodeling of ESCRT-III assemblies that lead to membrane constriction and scission (16). Polymerization of CHMP4 is considered a major driver of scission; however, this is held in check by capping with CHMP2 (41). VPS4 can solubilize CHMP2 subunits, allowing CHMP4 growth to progress, leading to scission (42). VPS4 binds to most of the MIM-containing CHMPs, including IST1 and CHMP1; however, CHMP2 is not known to have a role in normal topology scission, and CHMP1 and IST1 are not known to engage in capping. Therefore, it is not clear whether the VPS4-driven decapping mechanism established in reverse topology membrane scission has any role in normal topology scission.

Spastin belongs to the same meiotic clade of AAA^+ ATPases as VPS4 and is best known as a microtubule-severing enzyme (43, 44). Mutations of the spastin (SPG4 and SPAST) gene are the main causes in patients suffering from hereditary spastic paraplegia (45). The spastin linkage to CHMP1B and IST1 is involved in the scission of recycling endosomal tubules (27). Disruption of any of these interactions increases endosomal tubulation, mistrafficking of cargoes, and dysregulation of proper lysosomal functions (25–27). It has remained unclear whether spastin can substitute for the possible scission or disassembly functions of VPS4 with respect to CHMP1B- and IST1-containing membrane tubes, in addition to its canonical microtubule-severing activity.

Recent cryo-EM reconstructions on synthetic liposomes showed that the polymerization of IST1 on the exterior of CHMP1B-coated tubes leads to a remodeling of the CHMP1B coat and tightly constricts the membrane but does not lead to membrane scission (24). Here, we used a powerful technique to assay ESCRT membrane scission in vitro by combining optical tweezers and fluorescence microscopy to visualize membrane nanotubes pulled from giant unilamellar vesicles (GUVs) (46, 47) and characterize the effect in addition of various ATPases on ESCRT dynamics. This assay allows for the formation of a positively curved membrane that mimics the membrane tubules where CHMP1B and IST1 bind. Using this highly sensitive and flexible system, we were able to reconstitute the scission reaction and delineate the roles of CHMP1B, IST1, VPS4, and spastin in normal topology scission.

Results

Binding and Constriction of CHMP1B and IST1 Do Not Cause Scission. We purified full-length CHMP1B and a truncated IST1 construct that spans residues 1 to 189 ($IST1^{NTD}$), which was previously shown to form tubular coats with enhanced helical order (24). CHMP1B and IST1 were incubated together with liposomes and visualized by cryo-EM, verifying that these are the minimal constructs to form protein-coated tubules (*SI Appendix*, Fig. S1). In order to probe the consequences of ESCRT-III binding on the membrane in real time, we employed a membrane tube pulling assay. We formed membrane nanotubes between aspiration pipet-immobilized GUVs (60% egg phosphatidylcholine (ePC) and 40% dioleoylphosphatidyserine (DOPS) with trace dioleoylphosphatidylethanolamine-ATTO488 (DOPE-ATTO488) and distearoylphosphatidyleth anolamin-PEG (2000)-biotin (DSPE-PEG-2000-Biotin)) and a streptavidin-coated bead by briefly putting them in contact and then pulling them apart. After pulling a tube, a second pipette filled with 5 μM ESCRT-III proteins LD555–CHMP1B and unlabeled $IST1^{NTD}$ (concentration in the pipette) was lowered and dispensed in proximity (20 to 30 μm) to the membrane tube. We monitored the reaction via fluorescence using confocal microscopy (Fig. 1*A* and *Materials and Methods*). Consistent with previous reports, LD555–CHMP1B immediately bound to membranes containing high negative charge density lipids (40 mol% phospatidylserine (PS)) (48) and constricted the membrane nanotubes (Fig. 1*B*). We observed membranes constricted to 25 ± 6 nm radii (mean ± SD) (Fig. 1*C*), as measured by lipid fluorescence (*SI Appendix*, Fig. S2). Although ESCRT-III binding alone constricted membrane tubes in this system, we did not observe scission of ESCRT-III–bound nanotubes ($n = 13$) under these conditions.

CHMP1B–IST1 Severs Membranes upon Dynamical Tube Extension. Since CHMP1B and IST1 can tubulate and scaffold the membrane, we asked whether these polymers are rigid

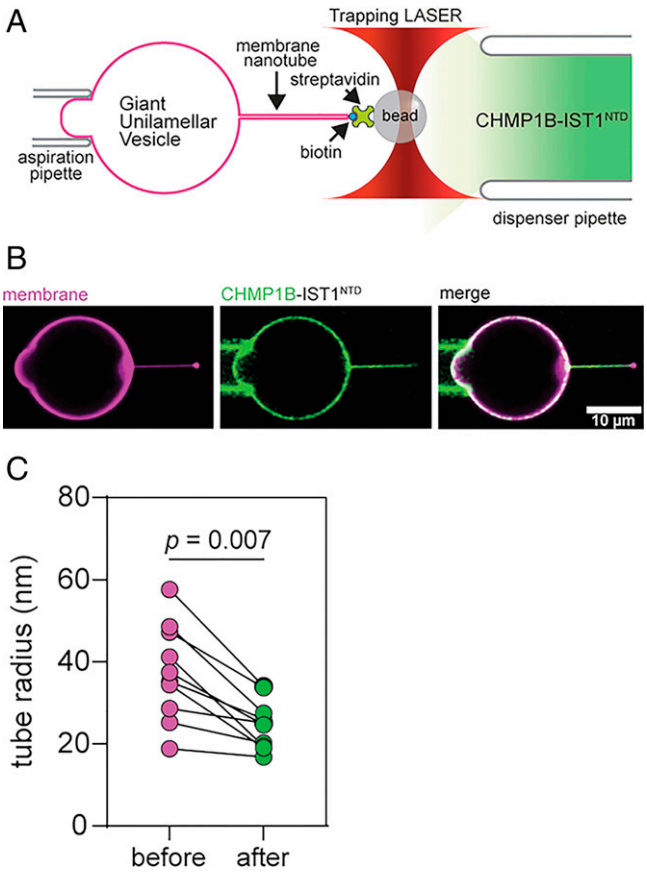

Fig. 1. ESCRT-III subunits CHMP1B and $IST1^{NTD}$ bind and constrict membranes. (*A*) Fluorescently labeled GUVs containing 59.4 mol% ePC, 40 mol% DOPS, 0.5 mol% DOPE-ATTO488, and 0.1 mol% DSPE-PEG-2000-biotin were held in place by suction using an aspiration pipette. Membrane nanotubes were formed between the immobilized GUV and a streptavidin-coated bead held by an optical trap after briefly putting them into contact and subsequently retracting them apart. (*B*) Representative confocal images showing LD555–CHMP1B (green) and $IST1^{NTD}$ on the tube after addition of 5 μM proteins on the membrane labeled with 0.5 mol% DOPE-ATTO488 (magenta). (*C*) Membrane tube diameter decreases upon binding of ESCRT-III proteins.

structures that could serve as lipid diffusion barriers and potentially promote friction-driven scission (FDS) (49). Fluorescence recovery after photobleaching (FRAP) was used to measure the dynamics of LD555–CHMP1B and IST1^{NTD} on GUVs. We initially incubated the GUVs with 500 nM LD555–CHMP1B and IST1^{NTD} followed by dilution to remove unbound proteins on the GUV. After incubation, GUVs show homogeneous CHMP1B coverage based on the fluorescence. After photobleaching a region on the GUV (Fig. 2*A*) we observed that fluorescence intensity did not recover after 2 min, indicating that the bound CHMP1B is immobile (Fig. 2*B*). We similarly performed FRAP experiments on the membrane, revealing that CHMP1B and IST1^{NTD} can act as a weak barrier that slows lipid diffusion (Fig. 2*C*).

We next asked whether formation of a rigid ESCRT-III coat can promote scission driven by friction with the tube membrane. To test this, we generated membrane nanotubes from GUVs using optical tweezers as above and subjected them to additional back and forth movements along the tube axis. As a control, we did not observe spontaneous scission of bare membranes upon axial motion (Fig. 3*A* and Movie S1). After

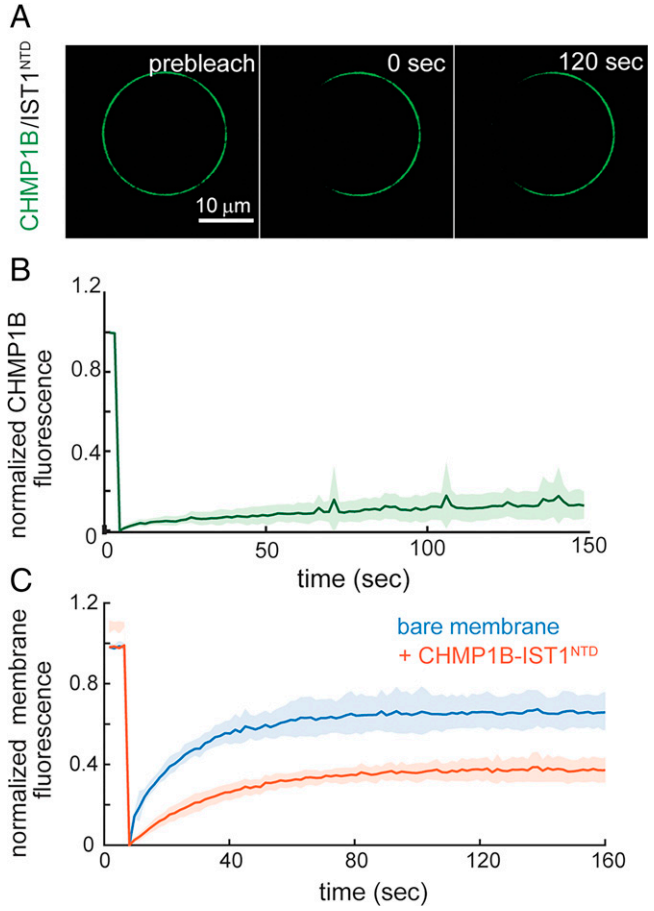

Fig. 2. CHMP1B and IST1^{NTD} form rigid structures on the membrane and act as a lipid diffusion barrier. (*A*) Representative image of LD555-labeled CHMP1B before and after performing FRAP to measure protein mobility on the membrane. A total of 500 nM LD555–CHMP1B and IST1^{NTD} were preadsorbed onto the GUV and diluted 5× to avoid recovery from soluble protein on the GUV from the external solution. (*B*) Recovery curve of LD555–CHMP1B showing that ESCRT-III subunits are immobile once bound on the membrane. Results are means ± SD from six FRAP experiments. (*C*) FRAP recovery curve of DOPE-ATTO647 after photobleaching on the GUV shows slow diffusion of lipids when proteins are bound (orange curve) compared to negative control measuring recovery of GUVs in the absence of proteins (blue curve). Results are means ± SD from six FRAP experiments.

CHMP1B and IST1 binding was established on the membrane tube, we pushed and pulled the tubes axially as before and observed scission as evidenced by loss of membrane fluorescence connecting the GUV and the bead. Formation of a rigid protein scaffold that can act as a lipid diffusion barrier on the tube is evident when we pushed the tube closer to the bead (Fig. 3*B*). Typically, two cycles of pushing and pulling were carried out over a distance of 30 μm at a speed of 3 μm s^{-1}. The presence of CHMP1B fluorescence seen at the end of the membrane tube five out of five trials suggests scission occurred at the edge of the protein scaffold (Fig. 3 *C* and *D*, Movie S2, and *SI Appendix*, Fig. S3). Therefore, membrane scission by ESCRT-III proteins can be promoted by applying an additional mechanical force through tube extension in the presence of a rigid protein scaffold.

Spastin Does Not Disassemble CHMP1B and IST1 from the Membrane. In reverse-topology ESCRT processes, the AAA$^+$ ATPase VPS4 is critical in the disassembly and remodeling of ESCRTs (50). VPS4 is thought to drive the constriction and eventual scission (16) of membranes by continuously removing the CHMP2 cap (42). Spastin belongs to the meiotic clade of AAA$^+$ ATPase together with VPS4 and is recruited by CHMP1B and IST1 in the endosomal recycling pathway (25–27). Like VPS4, spastin contains a MIT domain that interacts with the MIM domain found on the C terminus of CHMP1B (51) and in full-length IST1 (26, 52, 53). Spastin predominantly exists as two isoforms in mammalian cells and acts primarily on microtubules (43, 54). Full-length spastin (M1-spastin) contains an N-terminal hydrophobic domain that tethers it to the endoplasmic reticulum (55). In contrast, the most abundant isoform, M87-spastin, is cytosolic and can be recruited to microtubules and early endosomes (27). Therefore, we purified M87-spastin and tested the stimulation of its ATPase activity by ESCRT-III proteins.

To assess whether spastin can extract CHMP1B from CHMP1B–IST1^{NTD} assemblies on membranes, we performed a GUV assay in which we incubated LD555–CHMP1B with IST1^{NTD} on GUVs containing 60 mol% ePC and 40 mol% DOPS for 30 min and then added it with spastin in solution (Fig. 4*A*). LD655–spastin bound to ESCRT-coated GUVs, but we did not observe any loss of fluorescence from CHMP1B, even after 30 min of incubation in the presence of 1 mM adenosine triphosphate (ATP), suggesting that the ESCRT coat is intact and stably bound on the membrane, just as in the buffer control (Fig. 4*B*). Altogether our data suggest that, although recruitment to CHMP1B is robust, spastin cannot uncoat CHMP1B from the membrane in vitro.

Spastin Binding and ATPase Stimulation by CHMP1B Does Not Sever Membrane Nanotubes. We found that spastin hydrolyses ATP at a rate of 28 ± 1 ATP/spastin·min and was slightly enhanced by soluble CHMP1B (Fig. 4*C*). There was no activation by a similar ESCRT-III protein, CHMP2A, which also has a VPS4-binding MIM domain (21, 22). Maximal ATPase activation of spastin was only observed in the presence of microtubules consistent with its main function in microtubule severing (*SI Appendix*, Fig. S4). We next examined whether this ATPase activity was required for scission of membranes bound with CHMP1B and IST1^{NTD} in vitro using the nanotube pulling assay. We introduced 5 μM spastin with 1 mM ATP using a third pipette at an angle close to the experimental region (Fig. 4*D*). This allows a controlled sequential delivery of spastin after initial binding of ESCRT-III proteins on preformed membrane

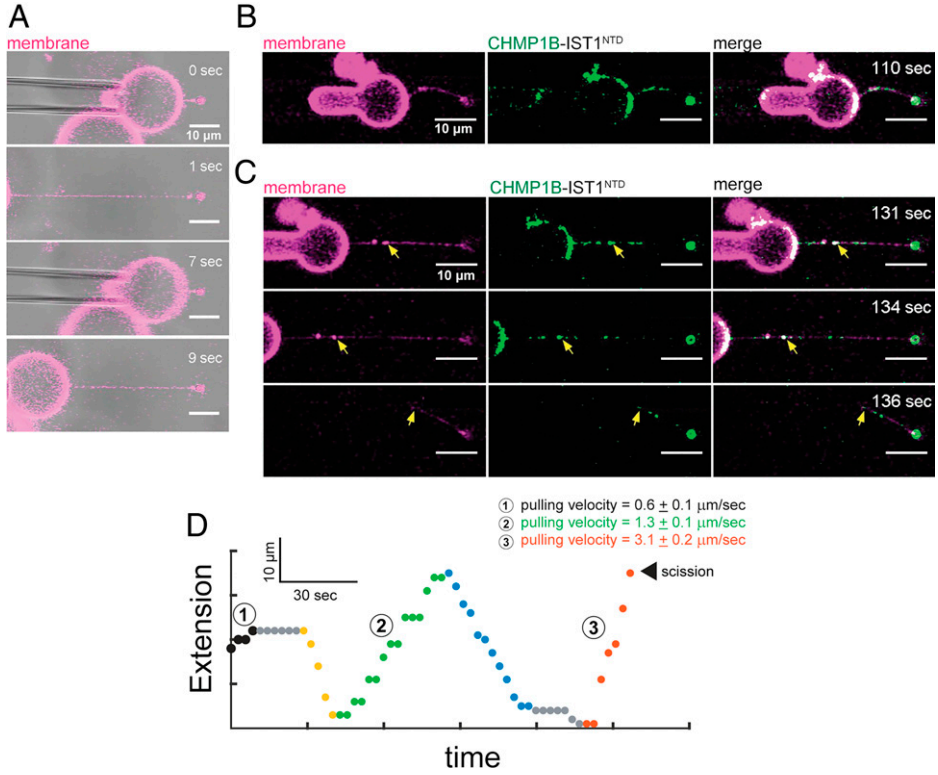

Fig. 3. External pulling on ESCRT-III scaffolded tubes promotes scission. (*A*) Bare membranes pulled at >25 μm·s^{-1} at 0.2 pN·nm^{-1} do not break even after repeatedly being brought back and forth. (*B*) Membrane tubes resisted retraction when pushed at 2 μm·s^{-1} after LD555–CHMP1B enrichment. (*C*) Snapshots of membrane tube, bound with LD555–CHMP1B-IST1^{NTD} protein, pulled at 3 μm·s^{-1} scaffolds induces scission. Yellow arrow highlights the point of scission. (*D*) Representative tube pulling trajectories of CHMP1B–IST1^{NTD} protein scaffolds on the tube. Pulling velocities below 3 μm·s^{-1} do not lead to scission (black and green circles) while pushing tubes at ~2 μm·s^{-1} (yellow and blue circles) show tube bending in *B*. Results are means ± SD from five experiments. (Scale bars, 10 μm.).

nanotubes (Movie S3). Spastin bound immediately to ESCRT-III on the tube after delivery as evidenced by strong colocalization of LD655–spastin to CHMP1B on the tube in all of our trials ($n = 4$) (Fig. 4*E*). This observation is consistent with previous reports of spastin colocalization to CHMP1B-enriched sites such as at the midbodies of dividing cells (51). However, in these experiments, carried out at constant tube length, we did not observe membrane scission even after more than 5 min (Movie S3). These data showed that direct interaction of spastin and CHMP1B is not sufficient to sever membranes.

VPS4 Uncoats Membrane-Bound ESCRT-III Proteins. Because VPS4 is the main ATPase tightly linked in canonical ESCRT processes, we asked whether VPS4 could promote disassembly of CHMP1B–IST1^{NTD} analogous to VPS4 activity on CHMP2–CHMP3 filaments (38, 42, 56). VPS4 has two paralogs, VPS4A and VPS4B, in mammalian cells, which have essentially equivalent functions. We focused on the VPS4B isoform for all our studies since we found that it is easier to express and purify. Human VPS4B has undetectable ATPase activity in the absence of substrate proteins (Fig. 5*A*). We observed that VPS4B activity was only marginally increased by CHMP1B (3.4 ± 0.9 ATP/VPS4B·min), while incubation with CHMP2A produced an ATP hydrolysis rate of 12.7 ± 0.4 ATP/VPS4B·min (Fig. 5*A*). Our data were consistent with previous findings that VPS4 engages the MIM domain of ESCRT-III proteins to stimulate its ATPase activity (21, 22, 57, 58).

We sought to determine whether VPS4 could disassemble and unfold CHMP1B–IST1. Treatment of preadsorbed LD555–CHMP1B and IST1 on GUVs with VPS4B and ATP led to uncoating of ESCRT proteins from the membrane, in contrast to GUVs with VPS4B omitted (Fig. 5 *B* and *C*). These findings confirm that VPS4B engages MIM1-containing ESCRT-III proteins and disassembles them, as expected.

ESCRT Disassembly by VPS4 Does Not Lead to Membrane Nanotube Scission. VPS4 is required for reverse topology scission by ESCRTs (16). We asked whether the presence of VPS4 and ATP could lead to scission using the tube pulling assay. To test this, we delivered 5 μM VPS4B and 1 mM ATP simultaneously at a low flow rate using a micropipette to prepulled nanotubes from GUVs after initial CHMP1B–IST1^{NTD} binding. Upon addition of VPS4B and ATP, we observed immediate loss of LD555–CHMP1B fluorescence intensity from the membrane, suggesting that the ESCRT protein was being uncoated (Fig. 5*D*). However, we observed rearrangement of LD555–CHMP1B intensity accumulating as a puncta at the junction of the tube and GUV (Fig. 5*D*) that seems refractory to VPS4/ATP treatment. This could be due to aggregation of CHMP1B and IST1^{NTD} that might hinder access by VPS4B. We did not see any evidence of membrane scission by VPS4B uncoating of CHMP1B from the membrane in any trial. These data suggest that VPS4 is not crucial for membrane scission on normal topology scission by CHMP1B and IST1 in vitro, although it may be essential for recycling of ESCRT-III back to the cytosolic pool.

Discussion

The membrane nanotube reconstitution reported here complements the recent cryo-EM study of Nguyen et al. (24). In combination, our observations provide a holistic account of the

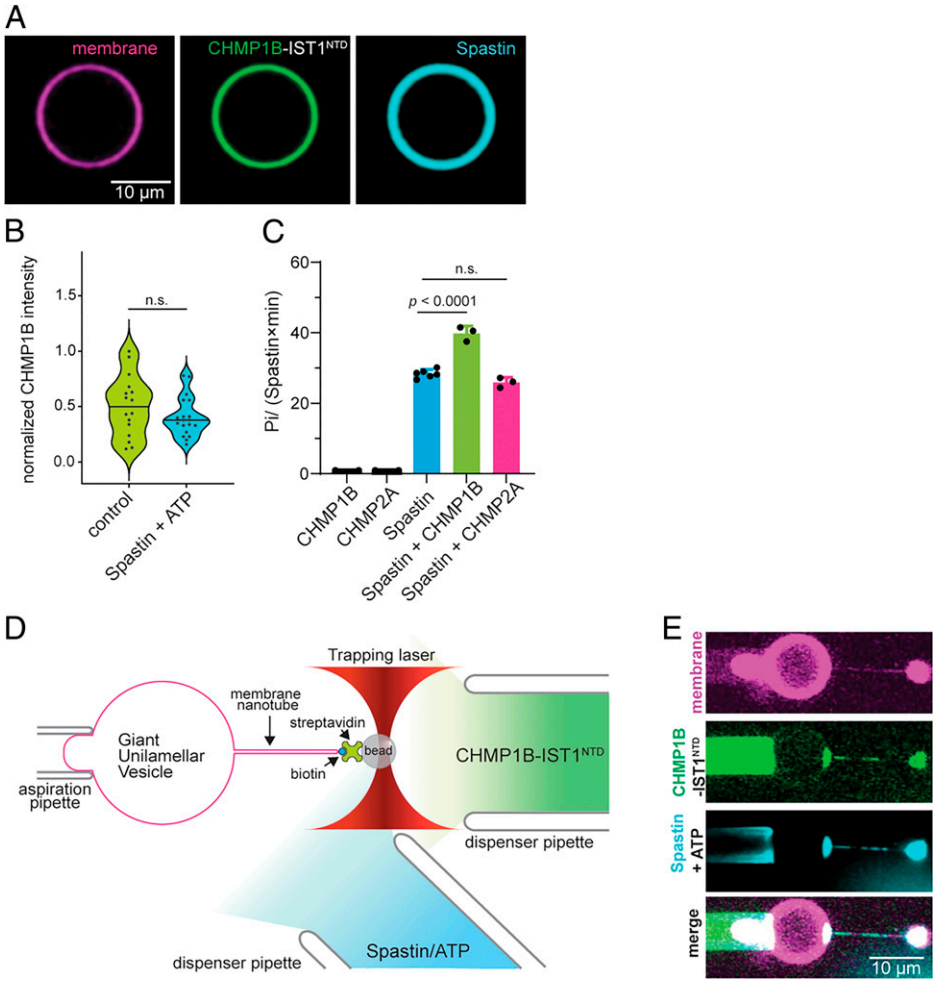

Fig. 4. Spastin colocalizes with ESCRT-III–enriched sites but does not uncoat or sever the membrane. (*A*) Representative image of GUVs labeled with DOPE-ATTO488 and preadsorbed with 500 nM LD555–CHMP1B and IST1^{NTD} after 30 min of incubation at room temperature with 500 nM LD655–spastin and 1 mM ATP. (Scale bar, 10 μm.) (*B*) Violin plot of the distribution of LD555–CHMP1B fluorescence on the GUV with or without 500 nM LD655–spastin and 1 mM ATP. (*C*) Spastin ATPase activity in the presence of ESCRT-III subunits. A total of 2 μM ESCRT-III subunits were incubated with 0.2 μM spastin and 2 mM ATP for 10 min at 37 °C. Spastin activity is mildly stimulated by CHMP1B but not by CHMP2A. At least three biological replicates were performed for each experimental condition. (*D*) Schematic representation of the tube pulling assay geometry as previously described but with the addition of a third pipette to dispense spastin and ATP. (*E*) Representative confocal images of LD655–spastin (cyan) colocalizing on LD555–CHMP1B (green) and IST1^{NTD}-enriched sites on the membrane (magenta). A total of 5 μM LD555–CHMP1B and 5 μM IST1^{NTD} were dispensed using a micropipette in proximity to the region of interest. A total of 5 μM spastin with 1 mM ATP was added after LD555–CHMP1B fluorescence equilibrated. No scission was observed in all of our trials (n = 4). (Scale bar, 10 μm.). n.s. = not significant.

action of ESCRT-III proteins CHMP1B and IST1 in the constriction and scission of positively curved membrane necks. As with any set of in vitro studies, we note the limitation that these experiments show what biological molecules are capable of doing, but not necessarily what they actually do in vivo. The IST1 MIM-domain interaction between either spastin or VPS4B MIT domains has recently been shown to be strong (K_D = 0.5 nM and 12 nM, respectively) (59) and its absence in our current reconstitution efforts may not completely capture its overall function and contribution in membrane scission. Both the cryo-EM and membrane nanotube studies find that the CHMP1B–IST1 coat strongly constricts membrane tubes but the constriction, by itself, does not lead to scission. The degree of constriction observed differed between the two studies. Here, we did not observe tube radii below 15 nm and therefore not sufficient to provide elastic energy to drive membrane scission (60), consistent with the absence of scission in the static tube-coating experiments. Our experiments used naturally occurring phosphatidylcholine with a mixture of 16:0, 18:0, 18:1, and 18:2 tails. Using cryo-EM, Nguyen et al. (24) reported that the gap between the inner leaflets of membrane tubes was narrowed by CHMP1B–IST1 coating to ∼5 nm. In order to achieve the highly constricted protein-coated tubules in the cryo-EM study, the asymmetric polyunsaturated (18:0 and 22:6) lipid, stearoyl-docosehexaenoyl-glycero-phosphocholine (SDPC) (61, 62) was used. Using brominated labels, this team found that the ends of the SDPC tails could be found near the membrane surface (63). The exceptional malleability of SDPC (59) probably explains why a high degree of constriction, yet not scission, was observed in the cryo-EM study. Our study shows that CHMP1B–IST1 coating is also capable of constricting membrane tubes of a more physiological composition, although it constricts them to a lesser degree.

We also sought to address the role of VPS4 and spastin in membrane scission. We found that VPS4 disassembles the ESCRT coat on the tubes, as expected. The major finding here is that VPS4 does not lead to scission in this reaction, nor is it required for friction-driven scission. The main role of VPS4 in reverse-topology scission is thought to be recycling of the CHMP2 cap to allow further rounds of CHMP4 polymerization

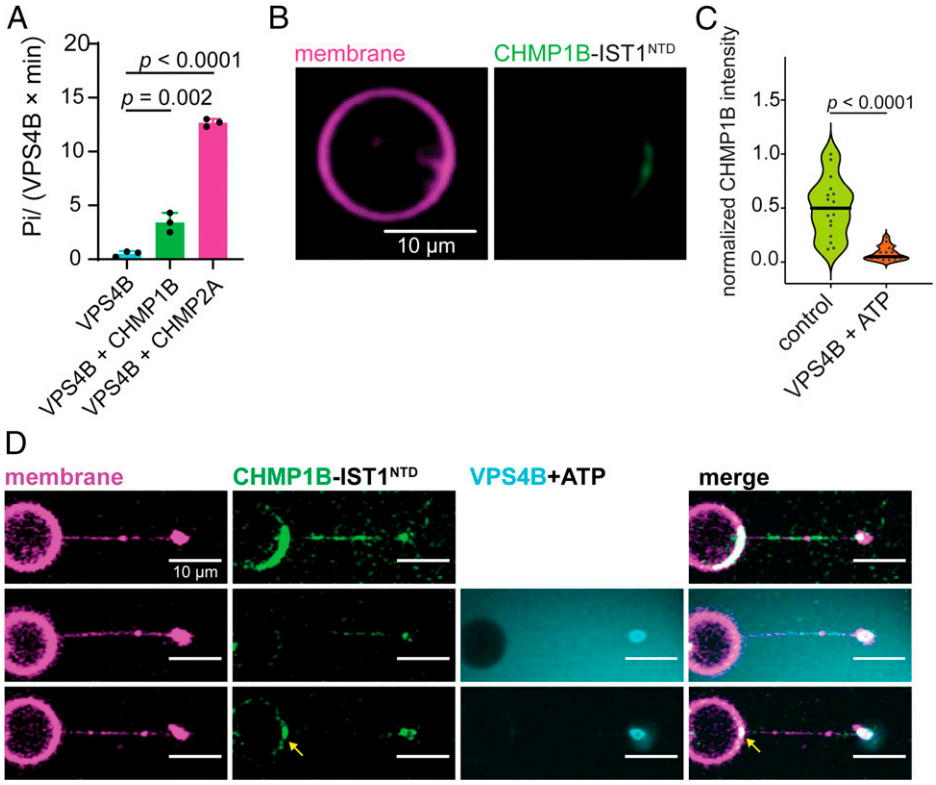

Fig. 5. VPS4 uncoats ESCRT-III but does not sever the membrane. (*A*) Rate of ATP hydrolysis by human VPS4B in the presence of full-length CHMP1B and CHMP2A. A total of 2 μM ESCRT-III subunit was incubated with 0.2 μM spastin and 2 mM ATP for 10 min at 37 °C. At least three biological replicates were performed for each experimental condition. (*B*) Representative image of GUVs labeled with DOPE-ATTO488 and preadsorbed with 500 nM LD555–CHMP1B and IST1^{NTD} after 30 min of incubation at room temperature with 500 nM VPS4B and 1 mM ATP. (Scale bar, 10 μm.) (*C*) Violin plot of the distribution of LD555–CHMP1B fluorescence on the GUV with or without 500 nM VPS4B and 1 mM ATP. (*D*) Snapshots of LD655–VPS4B and ATP disassembling LD555–CHMP1B and IST1^{NTD} from the membrane (magenta) without severing the tube. A total of 5 μM LD555–CHMP1B and 5 μM IST1^{NTD} were dispensed using a micropipette in proximity to the region of interest. A total of 5 μM VPS4B with 1 mM ATP was added after LD555–CHMP1B fluorescence equilibrated on the membrane. Yellow arrow points to presence of refractory LD555–CHMP1B that resisted VPS4B disassembly at the base of the tube. No scission was observed in all of our trials ($n = 3$). (Scale bar, 10 μm.).

(42). Since our system does not contain CHMP2, it is not surprising that VPS4 is not required for CHMP1B and IST1 polymerization on positively curved membranes. We asked whether spastin, like VPS4, could recycle CHMP1B subunits. The primary function of spastin in the cell is to sever microtubules using the energy released during ATP hydrolysis (44, 64–66). The recruitment of spastin via MIT interaction with MIM-containing ESCRT-III subunits and its ATPase activity are both essential for the regulation of endosomal tubules (25–27). We asked whether spastin could have a second role in disassembly of CHMP1B and IST1 from the membrane (54, 55). Our finding that spastin localizes on CHMP1B- and IST1-coated tubes was expected, given the tight interaction of spastin with CHMP1B. However, this interaction does not disassemble the coat or sever the membrane. These data are in contradiction to the long-standing speculation in the field that spastin could have a dual function as an ESCRT disassemblase. However, these data support the "standard model" that spastin is a microtubule-severing enzyme that can be localized within cells by ESCRTs (1, 26, 51), but is not itself an ESCRT disassemblase.

We found that membrane scission occurs on CHMP1B–IST1-coated tubes when an additional mechanical pulling force is applied. Pulling velocities of the order of 3 μm s^{-1} were used in this study, which exceed the minimum value of 1 μm s^{-1} previously reported for FDS by the endophilin coat (49). Pulling of the membrane under a rigid protein scaffold in this velocity regime leads to friction between the lipids and the scaffold. Exposed hydrophobic amino acid side chains from helix α1 of CHMP1B were found by molecular simulations based on the cryo-EM structure (24) to lead to "scoring" of the membrane surface and exposure of phospholipid hydrocarbon tails (63). These strong interactions presumably account for the friction between the inner surface of the CHMP1B coat and the membrane. A FDS mechanism has been proposed to explain dynamin-independent vesicle release by the N-BAR domain protein endophilin (49, 67), constriction of endoplasmic reticulum membranes by reticulon (68), as well as in membrane fission in bacteria (69). FDS mechanism has also been suggested for the fission and release of melanosomal tubules by myosin VI walking along actin filaments (70). In FDS, molecular motors operating on microtubules, such as dynein, contribute the pulling force. Scission occurs when membrane tubules are destabilized by micropores created when a protein scaffold prevents the equilibration of membrane tension by limiting the lipid flow underneath upon tube extension (49). Microtubules are closely connected to the biological pathways that involve CHMP1B–IST1 coating of tubular vesicles (25–29). Thus, it seems reasonable to hypothesize that such a process could account for membrane scission in these cases.

Our findings lead us to propose the following model for the role of spastin and VPS4 in normal topology membrane scission by ESCRT-III proteins (Fig. 6). Recruitment of CHMP1B to the membrane provides initial constriction, and IST1 binding further drives this constriction (Fig. 6 *A* and *B*). Simultaneously or subsequently, addition of some external force applied by microtubule-associated motor proteins can provide the necessary frictional force that leads to membrane scission (Fig. 6*C*).

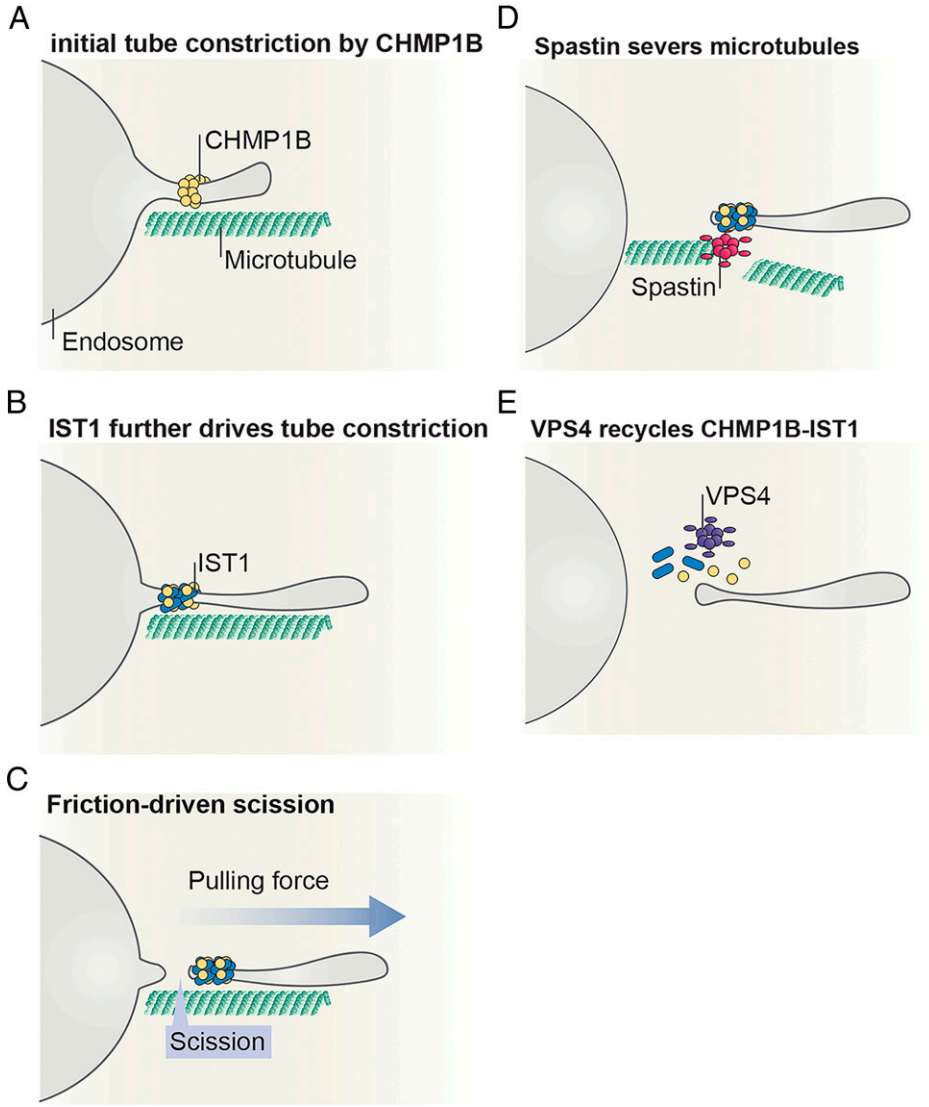

Fig. 6. Model for friction-driven scission by CHMP1B and IST1. (*A*) CHMP1B binds on the outer leaflet of endosome tubules forming a scaffold that constricts the positively curved tube. (*B*) As the tube continues to grow, IST1 gets recruited to the membrane forming an assembly with CHMP1B that further constricts the tube. (*C*) Tube elongation promoted by an external pulling force can induce scission by friction between the protein scaffold and the underlying membrane. (*D*) Spastin gets recruited to ESCRT-III–enriched sites and severs the microtubules surrounding the tube. (*E*) Finally, the AAA^+ ATPase VPS4 disassembles the ESCRT-III assembly back to the cytosol.

In parallel, recruitment of spastin to ESCRT-III–enriched sites severs the microtubules that run parallel with endosomal recycling tubes (51) (Fig. 6*D*); meanwhile, VPS4 uncoats CHMP1B and IST1 from the membrane back to the cytoplasmic pool (Fig. 6*E*). It remains to be seen what prevents spastin microtubule-severing activity and VPS4-mediated ESCRT disassembly until the necessary FDS reaction has been completed. This could be under kinetic control, or there could be additional levels of regulation to be discovered. These insights establish a biophysical basis for normal topology membrane severing by ESCRTs.

Materials and Methods

Reagents. The following lipids: L-α-phospatidylcholine (EPC, 840051C), 1,2-dioleoyl-*sn*-glycero-3-phosphocholine (DOPC,850375C), 1,2-dioleoyl-*sn*-glycero-3-phospho-L-serine (DOPS, 840035C), 1,2-distearoyl-*sn*-glycero-3-phosphoethanolamine-*N*-[biotinyl(polyethylene glycol)-2000] (DSPE-PEG(2000)Biotin, 880129C) were purchased from Avanti Polar Lipids, while 1,2-dioleoyl-*sn*-glycero-3-phosphoethanolamine-ATTO488 (DOPE-ATTO488, AD488-161) was purchased from ATTO-TEC. Lipid stock concentrations of 5 mg/mL were prepared by addition of chloroform from initial stocks of 10 mg/mL except for DOPE-ATTO488 where the lipid were solubilized in chloroform to a final concentration of 1 mg/mL. All lipids were kept under argon to avoid lipid oxidation and stored in −20 °C in amber vials.

Streptavidin-coated silica beads (diameter 1.56 μm) were purchased from Spherotech. All other reagents were purchased from Sigma-Aldrich unless otherwise specified.

Protein Expression, Purification, and Labeling. A single cysteine mutation at position 2 was introduced in the full-length human CHMP1B ($CHMP1B^{S2C}$), for fluorophore labeling with maleimide dye were fused to a tobacco etch virus (TEV) cleavable N-terminal His_6-MBP tag. A similar approach was followed for IST1 containing residues 1 to 189 ($IST1^{NTD}$). $CHMP1B^{S2C}$ and $IST1^{NTD}$ were transformed into *Escherichia coli* strain Rosetta (DE3) pLysS and grown in Luria-Bertani (LB) medium at 37 °C. Upon reaching 0.6 at OD_{600} cells were induced with 0.5 mM isopropyl β-D-1-thiogalactopyranoside (IPTG) for 16 h at 20 °C. Cells were pelleted, resuspended, and lysed in lysis buffer [50 mM Tris·HCl, pH 8.0; 500 mM NaCl; 20 mM imidazole; 0.5 mM Tris(2-carboxyethyl)phosphine (TCEP) supplemented with 1 mM phenylmethylsulfonyl fluoride (PMSF) and ethylenediaminetetraacetic acid (EDTA)-free protease inhibitors (Roche). The lysate was clarified by centrifugation and the proteins in the supernatant were purified by gravity Ni-nitrilotriacetic acid (Ni-NTA) affinity chromatography. The bound

proteins were washed extensively with lysis buffer (lacking protease inhibitor) and eluted with elution buffer (50 mM Tris·HCl, pH 8.0; 500 mM NaCl; 250 mM imidazole; 0.5 mM TCEP). The eluate was concentrated and then applied to an initial size-exclusion chromatography (SEC) step using HiLoad 16/60 Superdex 200 (GE Healthcare) in SEC200 buffer (50 mM Tris·HCl, pH 8.0; 150 mM NaCl, and 0.5 mM TCEP). Peaks corresponding to target protein were pooled and diluted 1.2- to 1.5-fold with SEC buffer followed by TEV cleavage at room temperature for 2 h. The pooled fractions were passed through a fresh 5-mL Ni-NTA resin to capture the His_6-MBP tag, TEV, and uncleaved proteins. The eluate was concentrated and applied to an SEC step using HiLoad 16/60 Superdex 75 (GE Healthcare) in SEC75 buffer (50 mM Tris·HCl, pH 7.4; 150 mM NaCl, and 0.5 mM TCEP). The highest peaks corresponding to the target protein were pooled and concentrated. The 2× molar excesses LD555 or LD655 (Lumidyne Technologies) were added to fluorescently label the protein. The protein and dye solution was rotated gently in a nutator at room temperature for 2 h and then at 4 °C overnight. Free dye was removed by passing the labeled protein through two 10DG desalting columns (Cytiva) and then through a Superdex75 10/300 size exclusion column. Proteins were flash frozen in liquid nitrogen and stored in a −80 °C freezer until use.

A codon-optimized synthetic gene for M87-spastin with a single-engineered cysteine at position 2 (^{M87}spastin^{A2C}) were fused to an N-terminal TEV cleavable His_6-GST tag and transformed and expressed in *E. coli* strain Rosetta (DE3) pLysS. The expression condition was similar to that described above. Cells were lysed by sonication in GST lysis buffer (50 mM Tris·HCl, pH 8.0, 500 mM NaCl, 5 mM $MgCl_2$, 0.5 mM TCEP, 10% glycerol, and 1 mM ATP) supplemented with 1 mM PMSF and EDTA-free protease inhibitor mixture. The cleared lysate was applied into glutathione-Sepharose 4B resin (GE Healthcare) overnight in 4 °C on a nutator. The resin was washed extensively with GST lysis buffer followed by incubation with 1 mM ATP to release contaminating bacterial ATPases, and then eluted with GST lysis buffer supplemented with 25 mM reduced glutathione. The eluent was diluted with IE-A buffer (50 mM Tris·HCl, pH 8.0, 0.5 mM TCEP) to have a final NaCl concentration of 75 mM before being applied to a 5-mL HiTrap SP HP cation chromatography column (Cytiva). The protein was eluted with a linear gradient of 75 mM to 1 M NaCl (IE-B, 50 mM Tris·HCl, pH 8.0, 1M NaCl, 0.5 mM TCEP). TEV was added to the pooled fractions and cleaved for 3 h at room temperature and passed through 5 mL Ni-NTA resin to capture TEV, His_6-GST tag, and uncleaved protein. The eluate was concentrated and applied to a SEC HiLoad 16/60 Superdex 75 column. The highest peaks corresponding to ^{M87}spastin^{A2C} were pooled, concentrated, flash frozen in liquid nitrogen, and stored in a −80 °C freezer until use. Protein labeling with LD655 was performed as described above.

Human VPS4B with a single mutation at position 2 for maleimide fluorophore labeling (VPS4B^{S2C}) was transformed and expressed as described above. Cells were lysed by sonication using lysis buffer with protease inhibitor mixture (50 mM Tris·HCl, pH 8.0, 500 mM NaCl, 5 mM $MgCl_2$, 20 mM imidazole, 0.5 mM TCEP, 10% glycerol, and 1 mM ATP) and applied into Ni-NTA beads. The bound protein on the resin was washed excessively with lysis buffer and incubated with 1 mM ATP for 30 min at room temperature to release contaminating bacterial ATPases. The protein was eluted with lysis buffer containing 250 mM imidazole. The NaCl concentration of the eluate was adjusted to 75 mM with IE-A buffer and applied to a 5-mL HiTrap Q Sepharose anion exchange column (GE Healthcare) and eluted with a linear gradient of 75 mM to 1 M NaCl (IE-B buffer). Fractions corresponding to VPS4B^{S2C} were pooled and labeled with 2× molar excess LD655 overnight. Excess dye was removed as described above. Protein was further purified by SEC using a HiLoad 16/60 Superdex 75 column. Protein was concentrated, flash frozen, and stored as described previously.

GUV Preparation. GUVs were prepared by hydrogel-assisted swelling as previously described. Briefly, 25 × 25 #2 coverslips were thoroughly rinsed while sonicating in water, then ethanol, then methanol, and finally in water. A total of 150 μL of 5% (wt/vol) polyvinyl alcohol with molecular weight of 145,000 (Millipore) was spin coated on plasma-cleaned coverslips. The thin polymer film was dried in an oven set to 60 °C for 30 min. A total of 15 μL of a 1 mg/mL lipid solution with the following mixture: 59.4% ePC, 40% DOPS, 0.5% DOPE-ATTO488, 0.1% DSPE-PEG-biotin was spread uniformly on the slide using a Hamilton syringe. The lipid film was dried for 1 h under high vacuum to remove excess solvent and rehydrated with growth buffer (20 mM Tris·HCl, pH 7.4; 40 mM NaCl; 160 mM sucrose) at room temperature for 45 min to 1 h. GUVs were harvested by pipetting from the slides and used immediately.

Optical Tweezers and Micropipette Manipulation Integrated to a Confocal Microscope. We made modifications from a previous custom-built optical trap on an inverted Nikon Ti-Eclipse microscope used to perform all our membrane tube pulling assays (16). Briefly, we use a collimated 5 W 1070 nm continuous-wave infrared laser beam (YLR-5-1080-Y12, IPG Photonics) tightly focused on the image plane by a Plan Apochromat 60× 1.2 numeric aperture (N.A.) water immersion objective (Nikon). The laser power of the trap was controlled by a half-wave plate introduced in the optical train followed by a polarizing beam splitter (PBS) cube prior to entering the back aperture of the objective. Before entering the confocal microscope body, the beam was expanded with lenses in a 4f-configuration to slightly overfill the back aperture of the objective. The beam was then guided to the back port of the confocal microscope via two mirrors forming a periscope. The position of the trap in the *z* axis was adjusted to match the *z* focus of the scanning confocal unit. The position of the bead relative to the center of the trap was monitored using back focal plane interferometry (BFP), by imaging the BFP of the condenser on a quadrant photodiode (QPD) system (E4100, Elliot Scientific). The instrument was controlled and raw voltage data from the QPD were converted to trapping forces in real time using custom software written in LabVIEW. The trap stiffness (0.1 to 0.2 pN/nm range) was obtained from the Lorentzian fit to the power spectrum of position fluctuations of the trapped bead. Brightfield illumination was provided by the top condenser unit and widefield fluorescence imaging light was introduced from the back port of the microscope (Sola SE II 365, Lumencor) to a videocamera positioned to the right camera port. Fluorescence imaging was controlled by NIS-Elements imaging software (Nikon).

Micromanipulators (MPC-145, Sutter Instrument) were attached on each side of the microscope stage and used to hold micropipettes. A custom open chamber holder was machined to accommodate insertion of micropipettes on either side of the chamber. Pressure inside the micropipettes was controlled by a high precision pressure controller (MFCS-EZ, Fluigent).

Malachite Green ATPase Activity Assay. All enzyme activity was determined by measuring the release of phosphate and formation of a green complex formed between malachite green oxalate with phosphomolybdate using the malachite green assay as previously described (55) with slight modifications and manufacturer specifications (Sigma-Aldrich). A total of 40 μL of ^{M87}spastin^{A2C} and VPS4B^{S2C} in ATPase buffer (20 mM Tris·HCl, pH 7.4, 100 mM KCl, 5 mM MgCl2, 0.5 mM TCEP) were aliquoted into a 96-well plate. Addition of 40 μL ESCRT-III protein or microtubule substrate in ATPase buffer supplemented with or without 2 mM ATP initiated the reaction. Final enzyme and protein concentrations in the reaction were 0.2 μM and 2 μM, respectively. The reaction mixture was incubated at 37 °C for 10 min and terminated by addition of 20 μL malachite green reagent. The reaction was further incubated for 60 min at room temperature prior to measuring absorbance with a plate-reading luminometer (GloMax, Promega). Samples were correlated to phosphate concentration standard controls. At least three biological replicates were performed for each experimental condition.

Fluorescence ATPase Activity Assay of ESCRTs on the GUV. GUVs were incubated with LD555–CHMP1B^{S2C} and IST1^{NTD} at a final concentration of 500 nM in experimental buffer (20 mM Tris·HCl, pH 7.4; 100 mM NaCl, 40 mM glucose, and 0.5 mM TCEP) for 15 min at room temperature. An eight-well observation chamber (Lab-Tek) was passivated with 5 mg/mL β-casein dissolved in experimental buffer for 30 min and rinsed three times. GUVs were then mixed with either spastin or VPS4B (final [enzyme] = 500 nM) in experimental buffer supplemented with 1 mM ATP and 1 mM $MgCl_2$ at room temperature in the observation chamber. Reaction mixtures were imaged after 30 min. At least three biological replicates were performed.

FRAP of ESCRTs and Membranes. GUVs with prebound ESCRTs were prepared similarly to the above description and subsequently diluted 5× in experimental buffer to avoid recovery from soluble protein in the GUV external solution. FRAP was performed with the excitation λ = 561 nm laser for LD555–CHMP1B^{S2C} or λ = 650 nm laser for DOPE-ATTO647 labeled membrane on a Nikon A1 confocal microscope with a 60× Plan Apochromat 1.4 N.A. oil immersion objective. A small rectangular region on the GUV with prebound ESCRTs was imaged at low laser

power (30 μW) for 3 to 5 s followed by 100% laser (15 mW) power for 15 to 30 s. Fluorescence recovery was imaged at low laser power over the course of 3 min. At least three biological replicates were performed.

Micropipette Preparation. Micropipettes made of borosilicate capillaries (inner diameter = 0.78 mm, outer diameter OD = 1 mm; B100-75-15, Sutter Instrument) were formed using a puller (P-1000, Sutter Instrument) and the tips were then microforged (MFG-5, MicroData Instrument) to an internal diameter of 4 to 5 μm for the GUV holder and 7 to 10 μm for dispenser pipettes.

Membrane Nanotube Pulling Assay. An open experimental chamber was formed by using two clean glass coverslips (VWR) separated by 1 mm on a custom-built chamber holder. The coverslips and interior of the micropipette used to hold the GUV were passivated with 5 mg/mL β-casein dissolved in experimental buffer for 30 min, rinsed three times, and filled with experimental buffer. A micropipette was filled with fluorescently labeled protein using a MicroFil flexible needle (MF34G-5, World Precision Instruments). The micropipettes were introduced on each side of the chamber and placed in the middle using micromanipulators. A third micropipette containing either spastin or VPS4B with or without ATP was inserted at an angle and all three pipettes were aligned in the same field of view. The pressure inside the pipette was adjusted so that no positive or negative flow was experienced inside the chamber. GUVs and streptavidin-coated silica beads were deposited in the chamber and allowed to settle. To form a membrane nanotube, a bead was held in place by an optical trap and briefly put in contact with a GUV aspirated on the pipette and held at low tension and then subsequently pulled away. Formation of the membrane nanotube was verified by fluorescence between the GUV and the bead and the sudden increase in force as measured by the optical trap. The chamber was sealed on each side by adding mineral oil to avoid evaporation.

Once a tube was formed, a micropipette was lowered into the field of view and protein was allowed to flow gently without disturbing the tube. After protein binding was established, the micropipette was raised up and another micropipette containing either spastin or VPS4 was lowered and injected into the field of view. All proteins were adjusted to match the osmolarity of the experimental buffer and verified using an osmometer (Osmette II, Precision Instruments).

Cryo-EM Sample Preparation. Lipids to form large unilamellar vesicles (LUVs) consisting of (55% SDPC, 20% DOPS, 10% brain $PI(4,5)P_2$, and 15% cholesterol, 2 mg total lipid) were dried in a round-bottom flask using a rotary evaporator at 55 °C. The resulting thin lipid film was further dried inside a vacuum desiccator overnight. Liposomes were prepared by rehydrating the lipid with buffer (20 mM Hepes, pH 7.5 and 100 mM NaCl) to a final concentration of 2 mg/mL and sonicated for 1 h at 55 °C followed by 10 freeze/thaw cycles. Lipids were then extruded 21 times through a 400-nm pore size filter or until the lipid suspension began to clarify, producing LUVs. LUVs (0.5 mg/mL) were mixed with 10 μM CHMP1B and $IST1^{NTD}$ and incubated overnight at room temperature.

Cryo-EM Data Collection. An incubated sample (3.5 μL) was applied to glow-discharged C-Flat Holey Carbon Grids (1.2/1.3, Au, 300 mesh). Grid blotting and vitrification were performed using a Vitrobot Mark IV (Thermo Fisher Scientific) (100% humidity, 22 °C, blot time = 5 s, blot force = 5) and Whatman 595 blotting paper.

Vitrified samples for cryo-EM were screened on a Talos Arctica (Thermo Fisher Scientific) with a Gatan K3 Summit direct detection camera in super-resolution counting mode with a pixel size of 0.4495 Å. Data were manually collected using SerialEM (71) and spanned a range of 2 to 5 μM defocus. Movies consisted of 50 frames, with a total dose of 85.2 $e^-/Å^2$ and a total exposure time of 10 s. Movie frames were motion corrected and dose weighted using MotionCor2 (72).

Statistical Analysis. Statistical analyses were performed with GraphPad Prism 9.0. Statistical differences for multiple comparisons were calculated by ordinary one-way ANOVA, Dunnett's multiple comparisons test. Single comparisons were calculated by Student's *t* test. For all plots with bars displayed, the error bars represent mean ± SD from at least three biological replicates performed independently. Calculated *P* values are displayed on each plot.

Data Availability. All microscopy movies are included in the supplementary data. Plasmids generated for this study will be deposited with Addgene (https://www.addgene.org/browse/article/28225151) (73). All other study data are included in the article and/or supporting information.

ACKNOWLEDGMENTS. We thank A. A. Garcia, S. Shukla, K. Rose, and L. Jensen for critical reading of the manuscript; the rest of the J.H.H. laboratory for insightful discussions; R. Tan for assistance with the microtubule disassembly assay; and L. Ferro for initial support with poly(dimethyl)siloxane and spin-coating procedure. We would also like to thank S. Velazquez for assistance with manufacturing custom microscope parts. This work was supported by NIH grants R37 AI112442 (J.H.H.), F31 AI150312 (A.K.C.), F32 AI155226 (K.P.L), and a Mayent-Rothschild visiting professorship at the Institut Curie (J.H.H.).

Author affiliations: [a]Department of Molecular and Cell Biology, University of California, Berkeley, CA 94720; [b]California Institute for Quantitative Biosciences, University of California, Berkeley, CA 94720; [c]Graduate Group in Biophysics, University of California, Berkeley, CA 94720; [d]Department of Chemistry, University of California, Berkeley, CA 94720; [e]Laboratoire Physico-Chimie Curie, Institut Curie, Université Paris Sciences & Letters, CNRS UMR168, Sorbonne Université, Paris, 75005 France; [f]Department of Physics, University of California, Berkeley, CA 94720; [g]Howard Hughes Medical Institute, University of California, Berkeley, CA 94720; [h]Kavli Energy Nanoscience Institute, University of California, Berkeley, CA 94720; and [i]Helen Wills Institute of Neuroscience, University of California, Berkeley, CA 94720

1. M. Vietri *et al.*, Spastin and ESCRT-III coordinate mitotic spindle disassembly and nuclear envelope sealing. *Nature* **522**, 231–235 (2015).
2. J. H. Hurley, ESCRTs are everywhere. *EMBO J.* **34**, 2398–2407 (2015).
3. M. Babst, MVB vesicle formation: ESCRT-dependent, ESCRT-independent and everything in between. *Curr. Opin. Cell Biol.* **23**, 452–457 (2011).
4. J. G. Carlton, J. Martin-Serrano, Parallels between cytokinesis and retroviral budding: A role for the ESCRT machinery. *Science* **316**, 1908–1912 (2007).
5. M. L. Skowyra, P. H. Schlesinger, T. V. Naismith, P. I. Hanson, Triggered recruitment of ESCRT machinery promotes endolysosomal repair. *Science* **360**, eaar5078 (2018).
6. L. L. Scheffer *et al.*, Mechanism of Ca^{2+}-triggered ESCRT assembly and regulation of cell membrane repair. *Nat. Commun.* **5**, 5646 (2014).
7. M. Radulovic *et al.*, ESCRT-mediated lysosome repair precedes lysophagy and promotes cell survival. *EMBO J.* **37**, e99753 (2018).
8. A. J. Jimenez *et al.*, ESCRT machinery is required for plasma membrane repair. *Science* **343**, 1247136 (2014).
9. M. Colombo *et al.*, Analysis of ESCRT functions in exosome biogenesis, composition and secretion highlights the heterogeneity of extracellular vesicles. *J. Cell Sci.* **126**, 5553–5565 (2013).
10. J. Votteler, W. I. Sundquist, Virus budding and the ESCRT pathway. *Cell Host Microbe* **14**, 232–241 (2013).
11. J. H. Hurley, A. K. Cada, Inside job: How the ESCRTs release HIV-1 from infected cells. *Biochem. Soc. Trans.* **46**, 1029–1036 (2018).
12. J. McCullough, W. I. Sundquist, Membrane remodeling: ESCRT-III filaments as molecular garrotes. *Curr. Biol.* **30**, R1425–R1428 (2020).
13. J. Schöneberg, I. H. Lee, J. H. Iwasa, J. H. Hurley, Reverse-topology membrane scission by the ESCRT proteins. *Nat. Rev. Mol. Cell Biol.* **18**, 5–17 (2017).
14. M. Babst, D. J. Katzmann, E. J. Estepa-Sabal, T. Meerloo, S. D. Emr, Escrt-III: An endosome-associated heterooligomeric protein complex required for mvb sorting. *Dev. Cell* **3**, 271–282 (2002).
15. T. Wollert, C. Wunder, J. Lippincott-Schwartz, J. H. Hurley, Membrane scission by the ESCRT-III complex. *Nature* **458**, 172–177 (2009).
16. J. Schöneberg *et al.*, ATP-dependent force generation and membrane scission by ESCRT-III and Vps4. *Science* **362**, 1423–1428 (2018).
17. M. Babst, B. Wendland, E. J. Estepa, S. D. Emr, The Vps4p AAA ATPase regulates membrane association of a Vps protein complex required for normal endosome function. *EMBO J.* **17**, 2982–2993 (1998).
18. D. S. Johnson, M. Bleck, S. M. Simon, Timing of ESCRT-III protein recruitment and membrane scission during HIV-1 assembly. *eLife* **7**, 7 (2018).
19. H. Han *et al.*, Structure of Vps4 with circular peptides and implications for translocation of two polypeptide chains by AAA+ ATPases. *eLife* **8**, 8 (2019).
20. H. Han, C. P. Hill, Structure and mechanism of the ESCRT pathway AAA+ ATPase Vps4. *Biochem. Soc. Trans.* **47**, 37–45 (2019).
21. M. D. Stuchell-Brereton *et al.*, ESCRT-III recognition by VPS4 ATPases. *Nature* **449**, 740–744 (2007).
22. T. Obita *et al.*, Structural basis for selective recognition of ESCRT-III by the AAA ATPase Vps4. *Nature* **449**, 735–739 (2007).
23. J. McCullough *et al.*, Structure and membrane remodeling activity of ESCRT-III helical polymers. *Science* **350**, 1548–1551 (2015).
24. H. C. Nguyen *et al.*, Membrane constriction and thinning by sequential ESCRT-III polymerization. *Nat. Struct. Mol. Biol.* **27**, 392–399 (2020).
25. R. Allison *et al.*, Defects in ER-endosome contacts impact lysosome function in hereditary spastic paraplegia. *J. Cell Biol.* **216**, 1337–1355 (2017).
26. R. Allison, J. R. Edgar, E. Reid, Spastin MIT Domain Disease-Associated Mutations Disrupt Lysosomal Function. *Front. Neurosci.* **13**, 1179 (2019).
27. R. Allison *et al.*, An ESCRT-spastin interaction promotes fission of recycling tubules from the endosome. *J. Cell Biol.* **202**, 527–543 (2013).
28. C. L. Chang *et al.*, Spastin tethers lipid droplets to peroxisomes and directs fatty acid trafficking through ESCRT-III. *J. Cell Biol.* **218**, 2583–2599 (2019).
29. F. D. Mast *et al.*, ESCRT-III is required for scissioning new peroxisomes from the endoplasmic reticulum. *J. Cell Biol.* **217**, 2087–2102 (2018).

30. I. H. Lee, H. Kai, L. A. Carlson, J. T. Groves, J. H. Hurley, Negative membrane curvature catalyzes nucleation of endosomal sorting complex required for transport (ESCRT)-III assembly. *Proc. Natl. Acad. Sci. U.S.A.* **112**, 15892–15897 (2015).
31. N. De Franceschi *et al.*, The ESCRT protein CHMP2B acts as a diffusion barrier on reconstituted membrane necks. *J. Cell Sci.* **132**, jcs217968 (2018).
32. T. Muziol *et al.*, Structural basis for budding by the ESCRT-III factor CHMP3. *Dev. Cell* **10**, 821–830 (2006).
33. S. Shim, L. A. Kimpler, P. I. Hanson, Structure/function analysis of four core ESCRT-III proteins reveals common regulatory role for extreme C-terminal domain. *Traffic* **8**, 1068–1079 (2007).
34. S. Ghazi-Tabatabai *et al.*, Structure and disassembly of filaments formed by the ESCRT-III subunit Vps24. *Structure* **16**, 1345–1356 (2008).
35. P. I. Hanson, R. Roth, Y. Lin, J. E. Heuser, Plasma membrane deformation by circular arrays of ESCRT-III protein filaments. *J. Cell Biol.* **180**, 389–402 (2008).
36. Q. T. Shen *et al.*, Structural analysis and modeling reveals new mechanisms governing ESCRT-III spiral filament assembly. *J. Cell Biol.* **206**, 763–777 (2014).
37. G. Effantin *et al.*, ESCRT-III CHMP2A and CHMP3 form variable helical polymers in vitro and act synergistically during HIV-1 budding. *Cell. Microbiol.* **15**, 213–226 (2013).
38. S. Lata *et al.*, Helical structures of ESCRT-III are disassembled by VPS4. *Science* **321**, 1354–1357 (2008).
39. A. Bertin *et al.*, Human ESCRT-III polymers assemble on positively curved membranes and induce helical membrane tube formation (vol 11, 2663, 2020). *Nat. Commun.* **11**, 1-13 (2020).
40. J. Moser von Filseck *et al.*, Anisotropic ESCRT-III architecture governs helical membrane tube formation. *Nat. Commun.* **11**, 1516 (2020).
41. D. Teis, S. Saksena, S. D. Emr, Ordered assembly of the ESCRT-III complex on endosomes is required to sequester cargo during MVB formation. *Dev. Cell* **15**, 578–589 (2008).
42. B. E. Mierzwa *et al.*, Dynamic subunit turnover in ESCRT-III assemblies is regulated by Vps4 to mediate membrane remodelling during cytokinesis. *Nat. Cell Biol.* **19**, 787–798 (2017).
43. A. Roll-Mecak, R. D. Vale, Structural basis of microtubule severing by the hereditary spastic paraplegia protein spastin. *Nature* **451**, 363–367 (2008).
44. A. Roll-Mecak, R. D. Vale, The Drosophila homologue of the hereditary spastic paraplegia protein, spastin, severs and disassembles microtubules. *Curr. Biol.* **15**, 650–655 (2005).
45. C. Plaud *et al.*, Functional differences of short and long isoforms of spastin harboring missense mutation. *Dis. Model. Mech.* **11**, dmm033704 (2018).
46. B. Sorre *et al.*, Curvature-driven lipid sorting needs proximity to a demixing point and is aided by proteins. *Proc. Natl. Acad. Sci. U.S.A.* **106**, 5622–5626 (2009).
47. C. Prevost, F. C. Tsai, P. Bassereau, M. Simunovic, *Pulling Membrane Nanotubes from Giant Unilamellar Vesicles* (Jove-J Vis Exp, 2017), p. 130.
48. A. K. Pfitzner *et al.*, An ESCRT-III polymerization sequence drives membrane deformation and fission. *Cell* **182**, 1140–1155.e18 (2020).
49. M. Simunovic *et al.*, Friction mediates scission of tubular membranes scaffolded by BAR proteins. *Cell* **170**, 172–184.e11 (2017).
50. W. M. Henne, H. Stenmark, S. D. Emr, Molecular mechanisms of the membrane sculpting ESCRT pathway. *Cold Spring Harb. Perspect. Biol.* **5**, a016766 (2013).
51. D. Yang *et al.*, Structural basis for midbody targeting of spastin by the ESCRT-III protein CHMP1B. *Nat. Struct. Mol. Biol.* **15**, 1278–1286 (2008).
52. B. Renvoisé *et al.*, SPG20 protein spartin is recruited to midbodies by ESCRT-III protein Ist1 and participates in cytokinesis. *Mol. Biol. Cell* **21**, 3293–3303 (2010).
53. M. Agromayor *et al.*, Essential role of hIST1 in cytokinesis. *Mol. Biol. Cell* **20**, 1374–1387 (2009).
54. J. H. Lumb, J. W. Connell, R. Allison, E. Reid, The AAA ATPase spastin links microtubule severing to membrane modelling. *Biochim. Biophys. Acta* **1823**, 192–197 (2012).
55. J. W. Connell, C. Lindon, J. P. Luzio, E. Reid, Spastin couples microtubule severing to membrane traffic in completion of cytokinesis and secretion. *Traffic* **10**, 42–56 (2009).
56. B. Yang, G. Stjepanovic, Q. Shen, A. Martin, J. H. Hurley, Vps4 disassembles an ESCRT-III filament by global unfolding and processive translocation. *Nat. Struct. Mol. Biol.* **22**, 492–498 (2015).
57. S. A. Merrill, P. I. Hanson, Activation of human VPS4A by ESCRT-III proteins reveals ability of substrates to relieve enzyme autoinhibition. *J. Biol. Chem.* **285**, 35428–35438 (2010).
58. A. Scott *et al.*, Structure and ESCRT-III protein interactions of the MIT domain of human VPS4A. *Proc. Natl. Acad. Sci. U.S.A.* **102**, 13813–13818 (2005).
59. D. M. Wenzel *et al.*, Comprehensive analysis of the human ESCRT-III-MIT domain interactome reveals new cofactors for cytokinetic abscission. *bioRxiv*. 2022:2022.02.09.477148.
60. Y. Kozlovsky, M. M. Kozlov, Membrane fission: Model for intermediate structures. *Biophys. J.* **85**, 85–96 (2003).
61. M. M. Manni *et al.*, Acyl chain asymmetry and polyunsaturation of brain phospholipids facilitate membrane vesiculation without leakage. *eLife* **7**, 7 (2018).
62. M. Pinot *et al.*, Lipid cell biology. Polyunsaturated phospholipids facilitate membrane deformation and fission by endocytic proteins. *Science* **345**, 693–697 (2014).
63. F. R. Moss *et al.*, Brominated lipid probes expose structural asymmetries in constricted membranes. *bioRxiv*. 2021:2021.08.24.457428.
64. K. J. Evans, E. R. Gomes, S. M. Reisenweber, G. G. Gundersen, B. P. Lauring, Linking axonal degeneration to microtubule remodeling by Spastin-mediated microtubule severing. *J. Cell Biol.* **168**, 599–606 (2005).
65. F. J. McNally, A. Roll-Mecak, Microtubule-severing enzymes: From cellular functions to molecular mechanism. *J. Cell Biol.* **217**, 4057–4069 (2018).
66. A. Errico, P. Claudiani, M. D'Addio, E. I. Rugarli, Spastin interacts with the centrosomal protein NA14, and is enriched in the spindle pole, the midbody and the distal axon. *Hum. Mol. Genet.* **13**, 2121–2132 (2004).
67. H. F. Renard *et al.*, Endophilin-A2 functions in membrane scission in clathrin-independent endocytosis. *Nature* **517**, 493–496 (2015).
68. J. Espadas *et al.*, Dynamic constriction and fission of endoplasmic reticulum membranes by reticulon. *Nat. Commun.* **10**, 5327 (2019).
69. A. Landajuela *et al.*, FisB relies on homo-oligomerization and lipid binding to catalyze membrane fission in bacteria. *PLoS Biol.* **19**, e3001314 (2021).
70. L. Ripoll *et al.*, Myosin VI and branched actin filaments mediate membrane constriction and fission of melanosomal tubule carriers. *J. Cell Biol.* **217**, 2709–2726 (2018).
71. D. N. Mastronarde, Automated electron microscope tomography using robust prediction of specimen movements. *J. Struct. Biol.* **152**, 36–51 (2005).
72. S. Q. Zheng *et al.*, MotionCor2: Anisotropic correction of beam-induced motion for improved cryo-electron microscopy. *Nat. Methods* **14**, 331–332 (2017).
73. A.K. Cada, *et al.*, Friction-driven membrane scission by the human ESCRT-III proteins CHMP1B and IST1. Addgene. https://www.addgene.org/browse/article/28225151. Deposited 22 April 2022.